

# Incorporating the algorithm for the boundary condition from FVM into the framework of Eulerian SPH

Zhentong Wang, Oskar J. Haidn, Xiangyu Hu\*

*TUM School of Engineering and Design, Technical University of Munich, Garching, 85747, Germany*

---

## Abstract

Finite volume method (FVM) is a widely used mesh-based technique, renowned for its computational efficiency and accuracy but it bears significant drawbacks, particularly in mesh generation and handling complex boundary interfaces or conditions. On the other hand, smoothed particle hydrodynamics (SPH) method, a popular meshless alternative, inherently circumvents the mesh generation and yields smoother numerical outcomes but at the expense of computational efficiency. Therefore, numerous researchers have strategically amalgamated the strengths of both methods to investigate complex flow phenomena and this synergy has yielded precise and computationally efficient outcomes. However, algorithms involving the weak coupling of these two methods tend to be intricate, which has issues pertaining to versatility, implementation, and mutual adaptation to hardware and coding structures. Thus, achieving a robust and strong coupling of FVM and SPH in a unified framework is imperative. Wang [2] has integrated mesh-based FVM into the SPH library SPHinXsys. However, due to differing boundary algorithms between these methods in Wang's work, the crucial step for establishing a strong coupling of both methods

---

\*Corresponding author.

*Email addresses:* zhentong.wang@tum.de (Zhentong Wang ), oskar.haidn@tum.de (Oskar J. Haidn), xiangyu.hu@tum.de (Xiangyu Hu )

within a unified SPH framework lies in incorporating the FVM boundary algorithm into the Eulerian SPH method. In this paper, we propose a straightforward algorithm in the Eulerian SPH method, algorithmically equivalent to that in FVM, grounded in the principle of zero-order consistency. Moreover, several numerical examples, including fully and weakly compressible flows with various boundary conditions in the Eulerian SPH method, validate the stability and accuracy of the proposed algorithm.

*Keywords:* Boundary algorithm, Finite volume method, Smoothed particle hydrodynamics, Strong coupling, Zero-order consistency, SPHinXsys

---

## 1. Introduction

In the context of rapidly advancing high-performance computing, computational fluid dynamics (CFD) has emerged as a highly promising method for addressing industrial challenges and has proven instrumental in elucidating longstanding flow phenomena across a spectrum of scales, ranging from microfluidics to hydrodynamics and hypersonics [6, 7]. While the traditional mesh-based CFD methods have undoubtedly achieved significant accomplishments, they exhibit drawbacks when confronted with complicated problems in practice. These challenges encompass the generation of high-quality meshes and the constraints arising from modelling complicated interfaces such as solid-fluid moving boundary [1] and violent deformations (e.g. wave breaking). Fortunately, for offering a solution to the latter constraints, the traditional mesh-based techniques, such as finite volume method (FVM), can be coupled with other numerical techniques, including mesh-based [8, 9, 10, 11] and meshless [12, 13, 3] methods and then enable obtaining convincing and accurate results. However, the former challenge is inherent in complex geometric settings within mesh-based methods. With the properties of avoiding the mesh generation and allowing large deformations during the simulations, the meshless methods have garnered

significant interest due to its numerical formulation being rooted in particles and not contingent on the topology defined by a mesh structure. As one of the typical meshless methods, smoothed particle hydrodynamics (SPH) method is characterized by numerical approximations grounded in Gaussian-like kernel functions [14, 15] and has found widespread application in diverse fields including CFD [16], structural mechanics [17], and various scientific and engineering domains [18, 19], particularly in scenarios where traditional mesh-based methods encounter challenges.

As previously indicated, numerous researchers have integrated FVM with meshless approaches to tackle intricate flows characterized by complex interfaces or boundaries. Similarly, they also have combined SPH with traditional mesh-based methods to enhance computational efficiency and address intricate boundary conditions, as documented in the literature [13, 3, 20]. Consequently, the fusion of mesh-based methods such as FVM and meshless methods such as SPH is of paramount significance for solving complex fluid dynamics problems. Nevertheless, it is essential to acknowledge that weakly coupling these multiple methods also introduces inherent limitations. Firstly, a potential concern pertains to the decreased numerical stability inherent in the amalgamation of two distinct methods when compared to the application of a single method, which arises from the necessity to formulate tailored algorithms for the purpose of data transfer or exchange within the overlapping regions or interfaces [12, 3, 21, 4]. Secondly, the implementation and generalization of coupling algorithms are intricate tasks [22], primarily owing to the inherent divergence in the fundamental characteristics of the coupled models. Thirdly, apart from variations in formulations, another notable challenge arises when attempting to couple methodologies that are tailored or extensively optimized for distinct types of hardware acceleration and coding constructs [22]. Hence, to address these intricate limitations, introducing a single framework for computing complicated CFD prob-

lems emerges as an imperative challenge that requires resolution. Following Ref. [2], Wang has proposed a certain form of Eulerian SPH method equivalent to FVM and implemented mesh-based FVM within an open-source SPH library (SPHinXsys), which paves the path of strong coupling these two methods within a unified SPH framework. While the both methods in the article [2] share the same discretized conservation equations and other techniques for improving the stability and accuracy, it is important to note that the treatment of boundary conditions varies between the particle-based and mesh-based approaches. Based on this, the incorporation of FVM boundary algorithm into Eulerian SPH method constitutes a pressing concern demanding immediate attention, as it not only enhances the equivalence between the Eulerian SPH and FVM but also constitutes a crucial component in establishing a robust and unified SPH framework for achieving a strong coupling between these two methods.

In this paper, by analysing the boundary algorithm in FVM where the each cell in the boundaries obeys the zero-order consistency, we propose a simple and general boundary algorithm adapted to Eulerian SPH method. During the process of implementing the boundary algorithm in FVM within the SPHinXsys, we create the extra storage and save the necessary data to keep the zero-order consistency for the particles within the boundaries missing several neighbouring particles. Besides, several numerical examples with a series of boundary conditions, including the reflecting, inflow, outflow, motionive, non-reflecting, non-slip wall and far-field boundary conditions, are tested in Eulerian SPH method to validate the stability and accuracy of the proposed algorithm.

The article is organized as follows: the governing equation and its discretization are given. Also, the dissipation limiters for improved accuracy and particle relaxation for the body-fitted particle distribution and zero-order consistency are

presented in Chapter 2. Besides, Chapter 3 explains the process of implementing the new boundary algorithm in Eulerian SPH in detail by comparing that in FVM. Finally, several examples with different boundary conditions are tested for the performance of the proposed algorithm in Chapter 4. The computational codes used in this study are readily available through the SPHinXsys repository [23, 24], which can be accessed via the following URLs: <https://www.sphinxsys.org> and <https://github.com/Xiangyu-Hu/SPHinXsys>.

## 2. Governing equations and Eulerian SPH method

### 2.1. Governing equations

The conservation equations within the Eulerian framework can be delineated as follows:

$$\frac{\partial \mathbf{U}}{\partial t} + \nabla \cdot \mathbf{F}(\mathbf{U}) = 0, \quad (1)$$

where  $\mathbf{F}(\mathbf{U})$  is the corresponding fluxes of  $\mathbf{U}$  denoting the vector of the conserved variables. In a two dimensional situation, they are expressed as

$$\mathbf{U} = \begin{bmatrix} \rho \\ \rho u \\ \rho v \\ E \end{bmatrix}, \quad \mathbf{F} = \begin{bmatrix} \rho u \\ \rho u^2 + p \\ \rho uv \\ u(E + p) \end{bmatrix} + \begin{bmatrix} \rho v \\ \rho vu \\ \rho v^2 + p \\ v(E + p) \end{bmatrix}, \quad (2)$$

where  $u$  and  $v$  are the components of velocity,  $\rho$  and  $p$  denote the density and pressure, respectively, as well as  $E = \frac{\rho v^2}{2} + \rho e$  is the total energy with  $e$  the internal energy. The equation of state (EOS) is introduced to close Eq. (1) as follows:

$$p = \begin{cases} \rho(\gamma - 1)e & \text{For compressible flows} \\ c^2(\rho - \rho_0) & \text{For weakly-compressible flows} \end{cases}. \quad (3)$$

Here,  $\gamma$  represents the heat capacity ratio, and  $\rho_0$  is the reference density. For compressible flows, we follow the ideal gas equation to derive the speed of sound:

$$c^2 = \frac{\gamma p}{\rho}. \quad (4)$$

In the case of incompressible flows, we adopt the weakly compressible assumption by employing an artificial EOS:

$$p = c^2(\rho - \rho_0). \quad (5)$$

To restrict density variations to within 1%, we define the speed of sound  $c = 10U_{max}$ , where  $U_{max}$  signifies the anticipated maximum velocity within the flow field. It is noteworthy that in this weakly compressible formulation, we turn off the energy conservation equation in Eq. (2).

## 2.2. Riemann-based Eulerian SPH discretization

In accordance with Ref. [25], we can express the discretized form of Eq. (1) as follows:

$$\begin{cases} \frac{\partial}{\partial t} (w_i \rho_i) + 2w_i \sum_j w_j (\rho \mathbf{v})_{E,ij}^* \cdot \nabla W_{ij} = 0 \\ \frac{\partial}{\partial t} (w_i \rho_i \mathbf{v}_i) + 2w_i \sum_j w_j [(\rho \mathbf{v} \otimes \mathbf{v})_{E,ij}^* + p_{E,ij}^* \mathbb{I}] \cdot \nabla W_{ij} = 0 \\ \frac{\partial}{\partial t} (w_i E_i) + 2w_i \sum_j w_j [(E \mathbf{v})_{E,ij}^* + (p \mathbf{v})_{E,ij}^*] \cdot \nabla W_{ij} = 0 \end{cases} \quad (6)$$

In this formulation,  $w$  signifies the particle volume,  $\mathbf{v}$  denotes the velocity,  $\mathbb{I}$  stands for the identity matrix, and  $\nabla W_{ij} = \frac{\partial W_{ij}}{\partial r_{ij}} \mathbf{e}_{ij}$  is the gradient of the kernel, where  $\mathbf{e}_{ij} = -\mathbf{r}_{ij}/r_{ij}$  and  $\mathbf{r}_{ij}$  represents the displacement vector pointing from particle  $j$  to  $i$ . Moreover, the terms  $(\ )_{E,ij}^*$  correspond to the solutions of the Riemann problem [25].

To solve the Riemann problem, we employ three waves characterized by varying speeds: the smallest denoted as  $S_l$ , the middle as  $S_*$ , and the largest as  $S_r$ . It is

important to note that the middle wave distinguishes between the two intermediate states, defined by  $(\rho_l^*, u_l^*, p_l^*)$  and  $(\rho_r^*, u_r^*, p_r^*)$ . For scenarios involving compressible flows, we opt for the HLLC Riemann solver [26, 27] due to its effectiveness in capturing shock discontinuities. The estimation of the smallest and largest wave speeds are as follows:

$$S_l = \tilde{u} - \tilde{c}, S_r = \tilde{u} + \tilde{c}, \quad (7)$$

where  $\tilde{u}$  and  $\tilde{c}$  denoting the density-average particle and sound speed replacing the Roe-average variables in Refs. [26, 27] can be expressed as

$$\begin{cases} H_l = \frac{E_l + p_l}{\rho_l}, H_r = \frac{E_r + p_r}{\rho_r}, \tilde{H} = \frac{\rho_l H_l + \rho_r H_r}{\rho_l + \rho_r}, \\ \tilde{u} = \frac{\rho_l u_l + \rho_r u_r}{\rho_l + \rho_r}, \tilde{c} = \sqrt{(\gamma - 1)(\tilde{H} - 0.5\tilde{u}^2)} \end{cases}, \quad (8)$$

with  $H$  representing the enthalpy. The middle wave speed can be further obtained by

$$S_* = \frac{\rho_r u_r (S_r - u_r) + \rho_l u_l (u_l - S_l) + p_l - p_r}{\rho_r (S_r - u_r) + \rho_l (u_l - S_l)}. \quad (9)$$

Subsequently, we can deduce the remaining states within the star region as follows:

$$p^* = p_l + \rho_l (u_l - S_l) (u_l - u^*) = p_r + \rho_r (S_r - u_r) (u^* - u_r), \quad (10)$$

$$\mathbf{v}_{l/r}^* = u^* \mathbf{e}_{ij} + \left[ \frac{1}{2}(\mathbf{v}_l + \mathbf{v}_r) - \frac{1}{2}(u_l + u_r) \mathbf{e}_{ij} \right], \quad (11)$$

$$\rho_{l/r}^* = \rho_{l/r} \frac{(S_{l/r} - q_{l/r})}{(S_{l/r} - u^*)}, \quad (12)$$

$$E_{l/r}^* = \frac{(S_{l/r} - q_{l/r}) E_{l/r} - p_{l/r} q_{l/r} + p^* u^*}{S_{l/r} - u^*}. \quad (13)$$

Here,  $u^*$  is equal to  $S_*$ , and  $q = un_x + vn_y$ , where  $n_x$  and  $n_y$  are components of the unit normal vector  $\mathbf{n}$ . For weakly compressible fluid flows, assuming that the intermediate states satisfy  $p_l^* = p_r^* = p^*$  and  $u_l^* = u_r^* = u^*$ , we can derive a linearized

Riemann solver [28] expressed by the following equations:

$$\begin{cases} u^* = \frac{u_l + u_r}{2} + \frac{1}{2} \frac{(p_l - p_r)}{\bar{\rho} \bar{c}} \\ p^* = \frac{p_l + p_r}{2} + \frac{1}{2} \bar{\rho} \bar{c} (u_l - u_r) \end{cases}. \quad (14)$$

Here,  $\bar{\rho}$  and  $\bar{c}$  represent averages.

To decrease the numerical dissipation, the limiter in the HLLC Riemann solver for compressible flows is introduced [2, 29] and the middle wave speed  $S_*$  and the pressure in the star region can be given by

$$\begin{cases} u^* = \frac{\rho_l u_l c_l + \rho_r u_r c_r}{\rho_l c_l + \rho_r c_r} + \frac{p_l - p_r}{\rho_l c_l + \rho_r c_r} \beta_{HLLC}^2 \\ p^* = \frac{p_l + p_r}{2} + \frac{1}{2} \beta_{HLLC} [\rho_r c_r (u^* - u_r) - \rho_l c_l (u_l - u^*)] \end{cases}. \quad (15)$$

Here, the limiter can be derived by

$$\beta_{HLLC} = \min \left( \eta_{HLLC} \left| \frac{u_l - u_r}{\bar{c}} \right|, 1 \right). \quad (16)$$

with  $\eta_{HLLC} = 1$ .

As for the weakly compressible flows, the middle wave speed and pressure in the linearised Riemann solver can be calculated as

$$\begin{cases} u^* = \frac{u_l + u_r}{2} + \frac{1}{2} \frac{(p_L - p_R)}{\bar{\rho} \bar{c}} \beta_{linearisd}^2 \\ p^* = \frac{p_l + p_r}{2} + \frac{1}{2} \beta_{linearisd} \bar{\rho} \bar{c} (u_l - u_r) \end{cases}, \quad (17)$$

where the limiter can be given by

$$\beta_{linearisd} = \min \left( \eta_{linearisd} \max \left( \frac{u_l - u_r}{\bar{c}}, 0 \right), 1 \right), \quad (18)$$

with  $\eta_{linearisd} = 15$ .

### 2.3. Particle relaxation technique

In practical phenomena with complex geometries, as the particle distribution with lattice is not sufficient, we implement particle relaxation [30] to make the particles fit precisely on the surface of the complex geometry.



The geometry is imported before particle relaxation and the initial particles with lattice distribution are physically driven by a constant background pressure written as

$$\mathbf{a}_i = -\frac{2}{\rho_i} \sum_j V_j \nabla W_{ij}. \quad (19)$$

When the acceleration reaches zero, the particles not in the boundaries attain stable positions and fulfill the condition of zero-order consistency, which can be expressed as  $\sum_j V_j \nabla W_{ij} = \mathbf{0}$ . It is noteworthy that particles located at the boundaries do not meet the zero-order consistency criteria. The resolution to this issue, specifically the implementation of eulerian boundary algorithm to rectify it, will be elaborated upon in the forthcoming section 3.

### 3. General boundary algorithm within Eulerian SPH

In this section, we elucidate the comprehensive general boundary algorithm within Eulerian SPH method through a comparative analysis with the boundary properties found in mesh-based FVM.

Following Refs. [2, 31], the discretized conservation Eq. (6) in both methods can be expressed uniformly as follows:

$$\frac{\partial}{\partial t} (\omega_i \mathbf{U}_i) + \sum_j \mathbf{F}_{ij}(\mathbf{U}) \cdot \mathbf{A}_{ij} = 0, \quad (20)$$

with  $j$  the neighboring cell or particle of  $i$ . Here,  $\mathbf{A}_{ij}$  denotes the size of the interface multiplying the normal unit vector to the interface and determines the flux contribution from cell or particle  $j$  among the total flux contributed by all neighboring cells or particles. Here, we categorize all cells in FVM and particles in Eulerian SPH into two groups: those within the boundaries and those outside the boundaries. Particularly, in FVM or in the following proposed boundary algorithm within Eulerian SPH

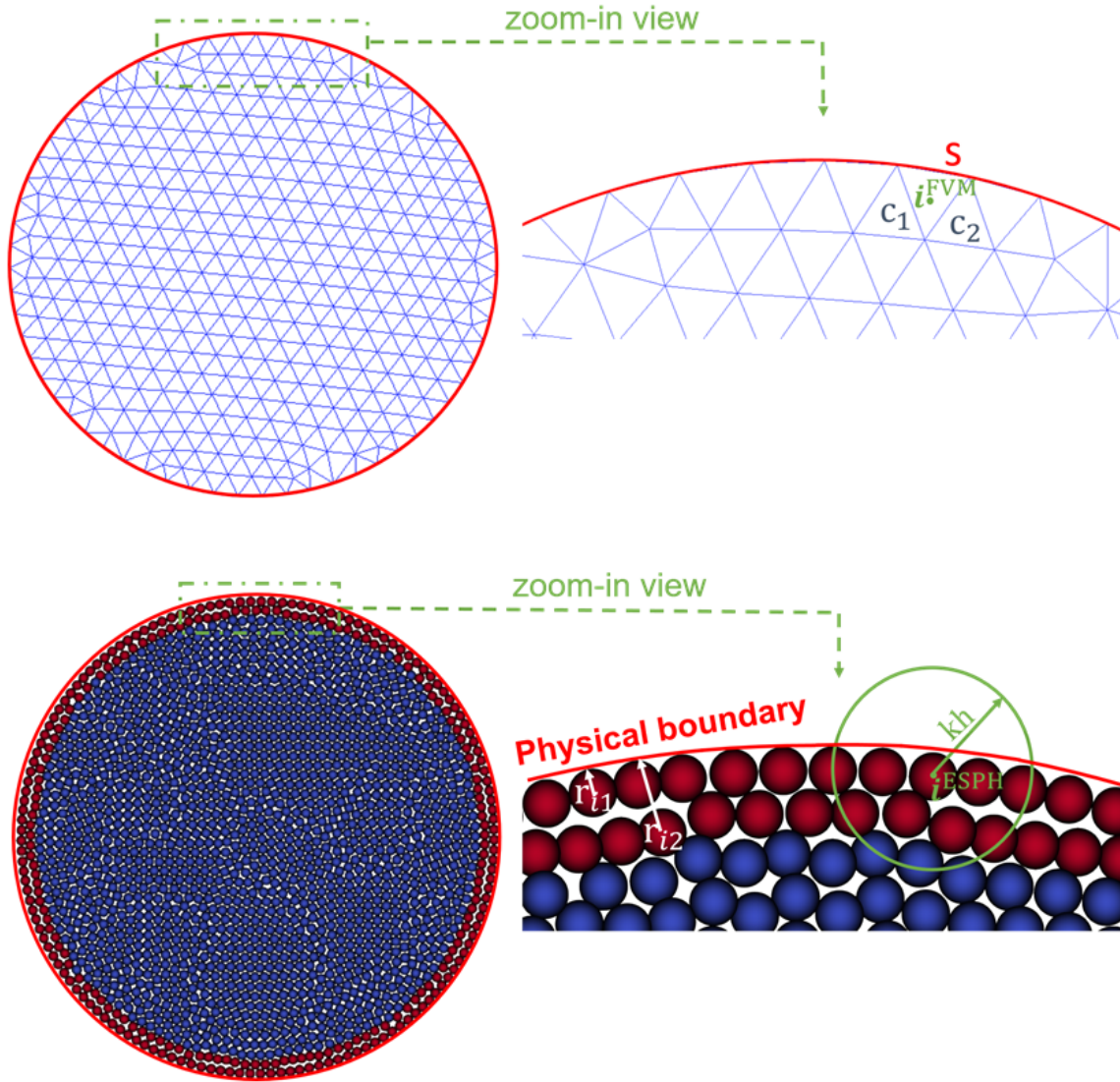


Figure 1: Mesh (top panel) and particle (bottom panel) distributions and their zoom-in views in FVM and Eulerian SPH, respectively, within a circular geometry. Note that the red circular line is the surface of the geometry.

method, for cells or particles located in the boundaries, we further subdivide the flux contribution from all cells and particles, denoted as label  $j$ , into two components: the contribution from neighboring particles or cells, denoted as label  $C$  in FVM and label  $P$  in Eulerian SPH method, within the interior in the subsequent discussion, and the contribution originating from the boundary surface, denoted as label  $S$  in the ensuing content.

In FVM, cells that do not intersect with the boundaries form self-contained control volumes [2, 31], which interact exclusively with their neighboring cells, inherently adhering to the condition  $\sum_j \mathbf{A}_{ij}^{FVM} = \mathbf{0}$ , i.e. naturally obeying the zero-order consistency. However, for cells situated along the boundary surface, such as cell  $i^{FVM}$  in Figure 1, a different approach is required. Here, the control volume must be closed off by the boundary surface shown by the red line in Figure 1 (top panel), with the size of this boundary surface determining the extent of flux contribution through it. With this boundary surface distribution, the cells within the boundaries continue to satisfy the zero-order consistency requirement. To clarify, the condition  $\sum_j \mathbf{A}_{ij}^{FVM} = \mathbf{0}$  of the cells within the boundaries can be rewritten as

$$\sum_j \mathbf{A}_{ij}^{FVM} = \sum_C \mathbf{A}_{iC}^{FVM} + \mathbf{A}_{iS}^{FVM} = \mathbf{0}. \quad (21)$$

Then, it is straightforward to derive the relation expressed as

$$\mathbf{A}_{iS}^{FVM} = - \sum_C \mathbf{A}_{iC}^{FVM}. \quad (22)$$

In Eulerian SPH, the SPH approximation relies on identifying neighboring particles within the compact support [14]. Once the particle relaxation process in Eq. (19) is completed, particles not within the boundaries conform to the zero-order consistency principle. However, for particles like particle  $i^{ESPH}$  located within the boundaries, as clearly depicted in Figure 1 (bottom panel), they lack neighboring

particles and thus fail to meet the zero-order consistency criteria. To address this issue, similar to Eq. (22), we introduce a surface vector along the normal direction to the boundary surface, which can be defined as follows:

$$\mathbf{A}_{iS}^{ESPH} = - \sum_P \mathbf{A}_{iP}^{ESPH}, \quad (23)$$

with  $\sum_p \mathbf{A}_{ip}^{ESPH} = \sum_p V_p \nabla W_{ip}$ . Following the inclusion of contributions from the boundary surface, particles within the boundaries adhere to the subsequent relationship:

$$\sum_j \mathbf{A}_{ij}^{ESPH} = \mathbf{A}_{iS}^{ESPH} + \sum_P \mathbf{A}_{iP}^{ESPH} = \mathbf{0}. \quad (24)$$

Here,  $j$  encompasses both neighboring particles and the boundary surface. Consequently, all particles within the computational domain achieve compliance with the zero-order consistency.

Now that we possess the algorithm for enforcing zero-order consistency in Eulerian SPH method, we proceed with the following steps for its implementation. The initial step involves distinguishing whether the particles reside within the boundaries. As indicated in Ref. [32, 33], we introduce the concept of the divergence of position, denoted as:

$$\nabla \cdot \mathbf{r}_i = \sum_j V_j \mathbf{r}_{ij} \cdot \nabla W_{ij}. \quad (25)$$

Here, particles within the full kernel support region satisfy  $\nabla \cdot \mathbf{r}_i \approx d$  with  $d$  denoting the dimension. In this context, we select a threshold value, denoted as  $\gamma$ , which is set at  $0.75d$  [33]. Consequently, a particle is categorized as residing within the boundaries when its divergence of position falls below this threshold value, and conversely, a particle is considered not to be within the boundaries. Based on this criterion, we identify the particles in the outer two layers that represented by the red particle layer in Figure 1 (bottom panel) as being within the boundaries. It is important to note

that in FVM, the boundary area corresponds to the outer surface of the geometry, as depicted in the top panel of Figure 1, which is analogous to the boundary area defined by the outermost two layers of particles in the geometry for Eulerian SPH method.

The second step is the computation of flux contribution originating from the boundary surface  $\mathbf{A}_{iS}^{ESPH}$  of each particle within the boundaries. Figure 2 provides flowchart diagrams detailing the configurations and the computation of flux contributions for variable updates using the original [29, 2, 34] and the proposed algorithms in Eulerian SPH in the case of fluid flows featuring varying boundary conditions. Diverging from the original approach, where two configurations, specifically the inner and contact configurations, are requisite for calculating flux contributions from both fluid and boundary particle components, the present algorithm demands only the inner configuration. Following the execution of the initial step, the particles within the boundaries can be appropriately labeled and the flux contributions of these boundary particles from their neighboring particles can be accurately calculated. Subsequently, in accordance with Eq. (24), the flux contribution arising from the boundary surface  $\mathbf{A}_{iS}^{ESPH}$ , as highlighted within the red dashed square in Figure 2, can be further obtained. Besides, the distance between these particles and the physical surface of the geometry denoted as  $r_{iS}$  similar with  $r_{i1}$  and  $r_{i2}$  in Figure 1 (bottom panel), can also be obtained easily in SPHinXsys.

The third step introduces an extra data storage space for the particles within the boundaries. This storage space is designed to retain essential information, encompassing the magnitude of the computed flux contribution from the boundary surface, i.e.  $|\mathbf{A}_{iS}^{ESPH}|$ , the normal unit vector to the boundary surface, i.e.  $\frac{\sum_p \mathbf{A}_{ip}^{ESPH}}{|\sum_p \mathbf{A}_{ip}^{ESPH}|}$ , the distance between the particle and the physical boundary surface, i.e.  $r_{iS}$ , and the input values of different boundary conditions. In the proposed algorithm, as shown

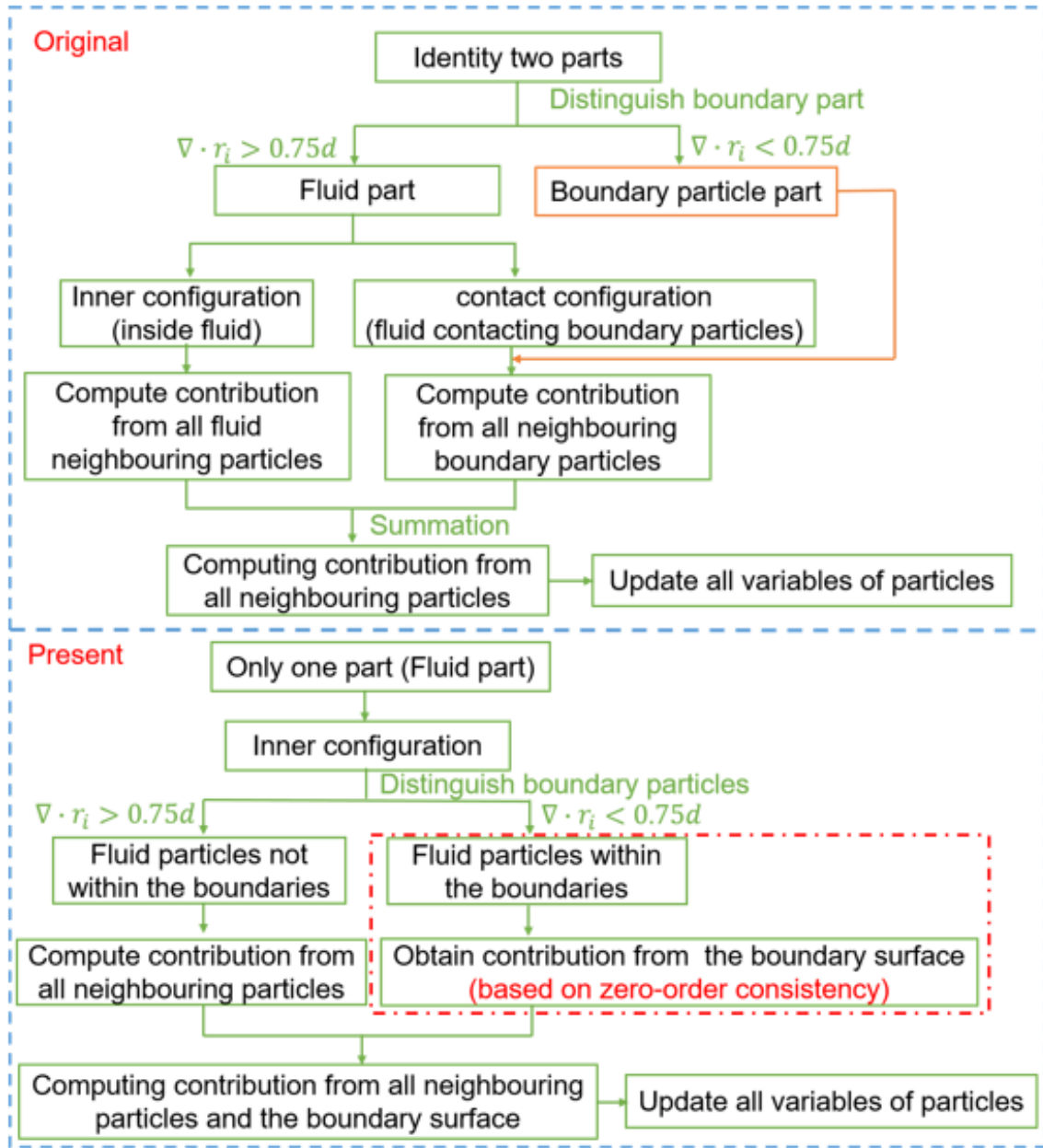


Figure 2: Flowcharts of the configurations in Eulerian SPH with the original algorithm labeled as "Original" in the top panel, and the proposed algorithm labeled as "Present" in the bottom panel are presented in the case of fluid flows with designed boundary condition. These flowcharts depict the process of computing contributions and updating variables at the new time based on the calculated contributions.

in the bottom panel of Figure 2, the inner configuration is divided into two parts including the inner neighbouring particles searched and the another configuration connecting with the boundary surface. In SPHinXsys, between a pairwise particle  $i$  and  $j$ , the kernel gradient  $\nabla W_{ij}$  multiplying the neighbouring particle volume, that is the flux contribution from the particle  $j$  to particle  $i$ , stored separately as the magnitude as  $\frac{\partial W_{ij}}{\partial r_{ij}} V_j$  and the displacement unit vector as  $\mathbf{e}_{ij}$ . Also, the displacement  $\mathbf{r}_{ij} = |\mathbf{r}_{ij}| \mathbf{e}_{ij}$  is stored as the magnitude  $|\mathbf{r}_{ij}|$  and replacement unit vector  $\mathbf{e}_{ij}$ . Based on this data structure, the flux contribution from the boundary surface of  $-\left|\sum_p \mathbf{A}_{ip}^{ESPH}\right|$  is stored in data storage of  $\frac{\partial W_{ij}}{\partial r_{ij}} V_j$  and normal unit vector to the boundary surface of  $-\frac{\sum_p \mathbf{A}_{ip}^{ESPH}}{\left|\sum_p \mathbf{A}_{ip}^{ESPH}\right|}$  is stored as  $\mathbf{e}_{ij}$ . Besides, the distance between the boundary particles and the physical surface of  $r_{iS}$  is stored in the data structure of  $|\mathbf{r}_{ij}|$ .

The fourth step entails the implementation of various boundary conditions. This algorithm exhibits a high level of generality, making it suitable for accommodating a wide array of boundary conditions such as the reflecting, inflow, outflow, motionive, non-reflecting, non-slip wall and far-field boundaries. For each boundary condition, we input the designated values of the boundary surface in the storage space. Since we have obtained the flux contributions from the the boundary surface separately in the third step, we can readily calculate the flux from the boundary surface with the given boundary condition. Subsequently, the total flux, encompassing contributions from neighboring particles and the boundary surface, can be obtained, and this information is used to update the variables for the new timestep. It is worth noting that in the original algorithm the boundary conditions were computed by relying on the many boundary particles in the contact configuration, whereas in the present algorithm the boundary conditions are computed by relying on the values of the

extra storage space in the inner configuration rather than the particles. Therefore, this boundary algorithm has the added benefit of reducing some computational effort as less neighbouring particles needed.

## 4. Numerical results

In this section, several numerical examples including fully and weakly compressible flows with the complicated geometries are studied to validate the stability and accuracy of the proposed boundary algorithm using different boundary conditions in Eulerian SPH method. In all cases, the truncated Laguerre-Gauss kernel [29] is applied for high accuracy with the cut-off radius as  $2.6dp$  where  $dp$  is the initial particle spacing.

### 4.1. A Mach 3 wind tunnel with a step

In this section, we delve into the examination of a Mach 3 inviscid flow around a two-dimensional forward-facing step. The primary objective is to validate the effectiveness of the proposed algorithm for handling boundary conditions, encompassing inflow, outflow, and reflective conditions, within this specific scenario. Following Refs. [35, 36, 37, 38], the wind tunnel in question boasts dimensions of one unit in width and three units in length. Positioned within this tunnel is a step, which is situated at a distance of 0.6 units from the tunnel's left-hand extremity and exhibits a height of 0.2 units. The left is the inflow boundary condition and the right is the supersonic outflow boundary condition with no effect on the flow, as well as the top and bottom are reflecting boundary conditions as is shown in Figure 3 which provides the geometry and boundary conditions.

Figure 4 illustrates the density contours over a range of 0.22 to 6.5, achieved using a spatial resolution of  $dp = 1/200$  at various time steps from  $t = 1$  to  $t = 4$ . This



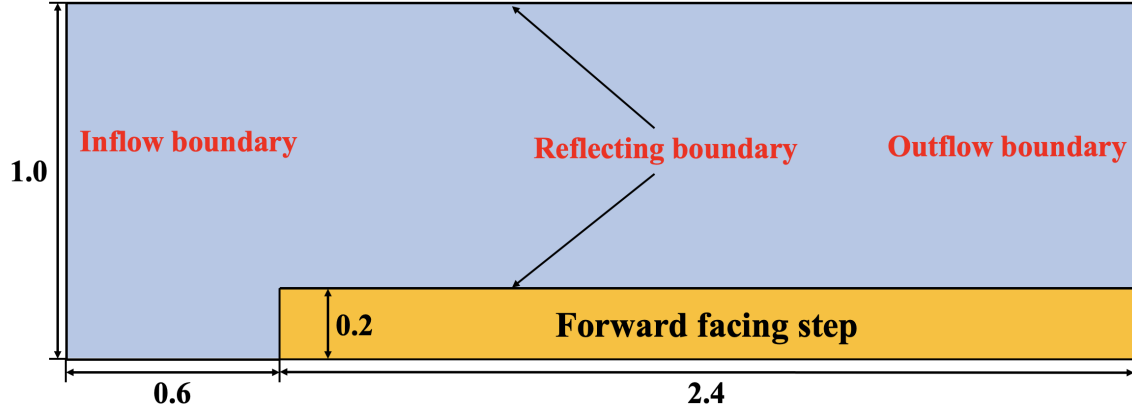


Figure 3: A Mach 3 wind tunnel with a step: The geometry and boundary conditions.

figure demonstrates the remarkable smoothness of the results obtained through the proposed boundary algorithm, thereby affirming the algorithm’s robustness. Moreover, it is worth noting that the density contours produced with this boundary algorithm closely align with findings from prior works, specifically those referenced in Refs. [35, 36, 37, 38], validating the accuracy and convincing of the proposed algorithm.

#### 4.2. Double Mach reflection of a strong shock

In this section, a two-dimensional inviscid flow, i.e. double Mach reflection of a strong shock, is tested to investigate the stability of the boundary algorithm with more complex boundary boundaries. The boundaries in this case contained various types including inflow, outflow, shock wave motion, and reflecting boundary conditions shown in Figure 5. Following Ref. [35], the conducted test pertains to a Mach 10 shock wave propagating through the air with a specific heat ratio  $\gamma$  of 1.4, and this shock wave forms a 60-degree angle with a reflective wall initially. Besides, the computational domain encompasses the region defined by  $(x, y) \in [0, 4] \times [0, 1]$ , and

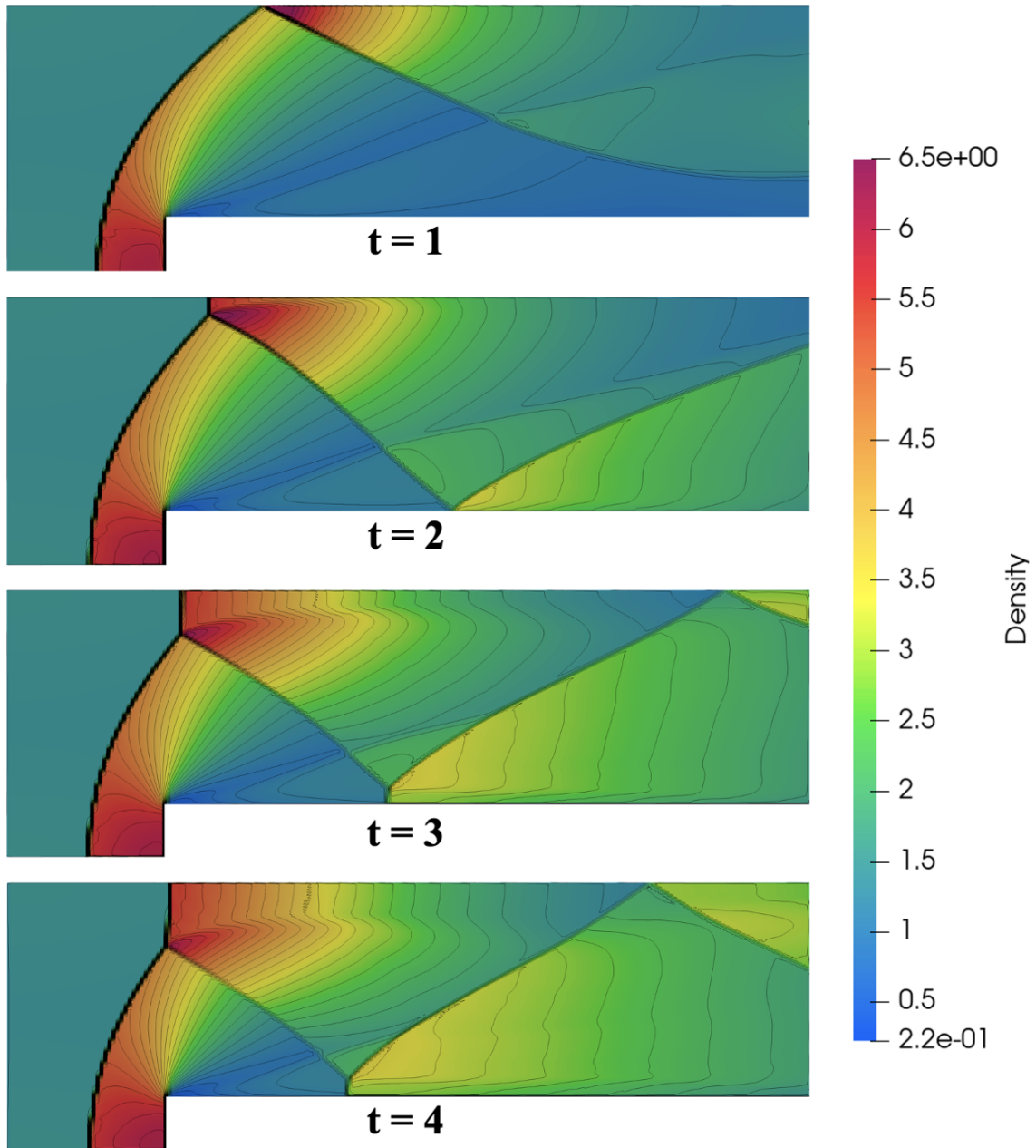


Figure 4: A Mach 3 wind tunnel with a step: 30 equally spaced density contour ranging from 0.22 to 6.5 with the spatial resolution  $dp = 1/200$  at the different instants including  $t = 1$  (top panel),  $t = 2$  (second top panel),  $t = 3$  (third top panel) and  $t = 4$  (bottom panel).

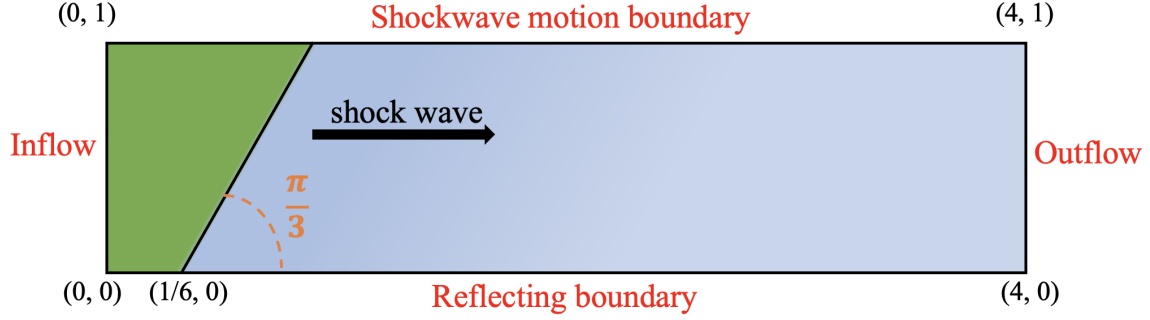


Figure 5: Double Mach reflection of a strong shock: The geometry and boundary conditions.

the initial condition is specified as follows:

$$(\rho, u, v, p) = \begin{cases} (1.4, 0, 0, 1) & y \leq 1.732(x - 0.1667) \\ (8, 7.145, -4.125, 116.8333) & \text{otherwise} \end{cases}, \quad (26)$$

with the final time as  $t = 0.2$  and the resolution is  $dp = 1/120$  to discretize the computational domain. Specifically, the bottom boundary is defined as a reflecting wall, initiating at  $x = 1/6$  where the shock is inclined at a 60-degree angle with respect to the x-axis. It extends vertically to the top of the domain at  $y = 1$ . The initial post-shock input boundary condition is applied from  $x = 0$  to  $x = 1/6$ . The left-hand boundary is set as the assigned value as the initial post-shock boundary condition, while the right-hand boundary is set to have zero-gradient output conditions. Moreover, for the top boundary, the variable is introduced to accurately describe the motion of the initial Mach 10 shock.

Figure 6 presents the density contour ranging from 1.1 to 23.0 under the resolution as  $dp = 1/120$  at the final time  $t = 0.2$ . It can be observed that the density contour is smooth using the different and complex boundary conditions and agrees well with the results in Refs. [35, 2], validating that the proposed boundary algorithm is stable and accurate.

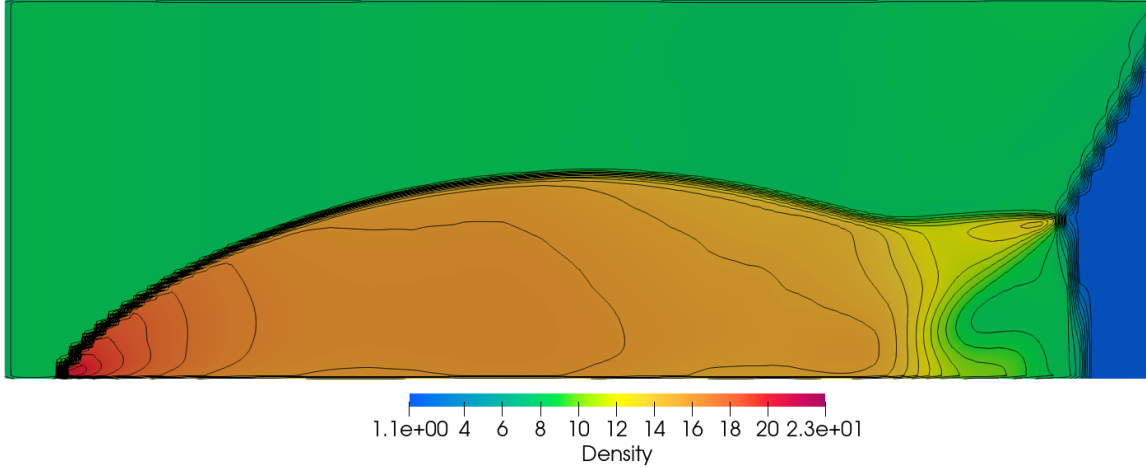


Figure 6: Double Mach reflection of a strong shock: 30 equally spaced density contour ranging from 1.1 to 23.0 with the spatial resolution  $dp = 1/120$  at the final time  $t = 0.2$ .

#### 4.3. Supersonic flow past a circular cylinder

In this section, we explore supersonic flow with complex geometry. Specifically, we simulate supersonic flow past a circular cylinder to assess the robustness of the proposed algorithm in handling intricate geometries under the different boundary conditions including non-reflecting and reflecting boundary conditions. Following Refs. [39, 40], the reflecting boundary condition is imposed on the cylinder surface, while the non-reflecting boundary conditions including supersonic inflow and outflow conditions are enforced at the other boundaries. In the case, the pressure and density inflows are set as  $\rho_\infty = 1.0$  and  $p_\infty = 1/\gamma$  with  $\gamma = 1.4$ , respectively. Besides, we configure the computational domain as a semi-circular geometry with a radius of  $5.5D$ , and the center of the inner cylinder is positioned at a distance of  $3.5D$  from the inflow boundary shown as Figure 7, with a cylinder diameter of  $D$  under the spatial resolution of  $dp = 1/20$  to discretize the computational domain.

Figures 8 and 9 show the pressure, density and velocity contours under the spatial

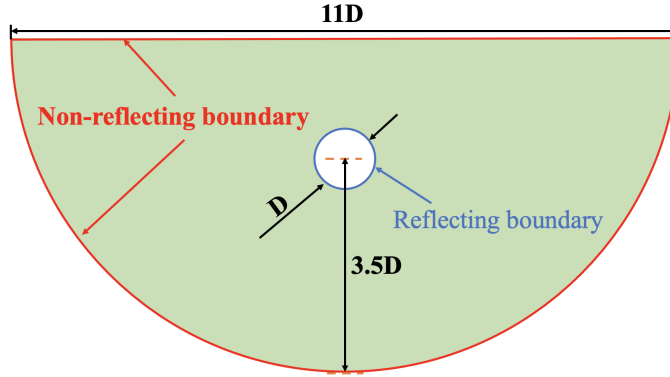


Figure 7: Supersonic flow past a circular cylinder: The geometry and boundary conditions.

resolution  $dp = 1/20$  with Mach = 2 and Mach = 3, respectively. It can be observed that the proposed boundary algorithm for non-reflecting and reflecting boundary conditions can obtain the smooth results and enable capture the shock property, representing its stability and accuracy. Besides, the results in Figures 8 and 9 agree well with the results in Refs. [39, 40] with Mach = 2 and Mach = 3, proving the results with non-reflecting and reflecting boundary conditions containing the complex geometry are convincing and correct.

#### 4.4. Flow around a circular cylinder

In this section, we investigate the impact of the proposed boundary algorithm in a two-dimensional viscous flow scenario, i.e. the flow around a circular cylinder. This problem features complex geometry and incorporates various boundary conditions, including non-slip wall and far-field conditions. As illustrated in Figure 10, which provides a depiction of the geometry and the distinct boundary conditions, we designate the circular surface as the non-slip wall boundary condition, while the remaining boundaries are configured as the far-field boundary condition. Following the approach outlined in Ref. [29], to mitigate the influence of the far-field boundary

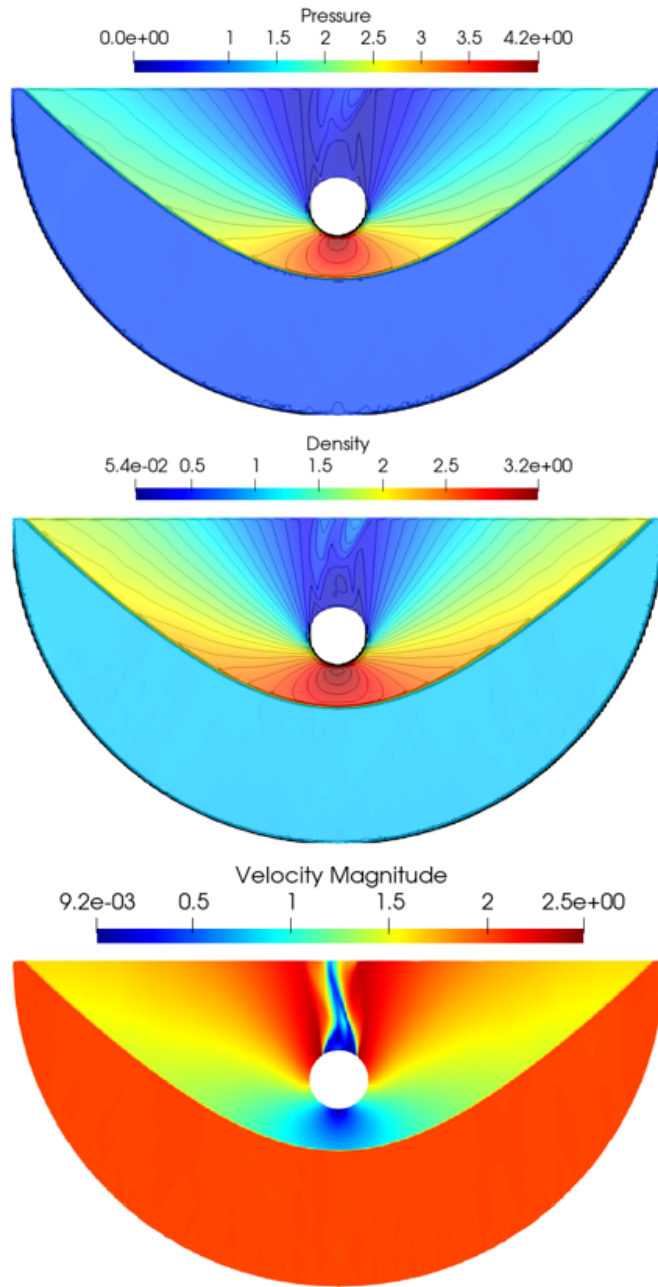


Figure 8: Supersonic flow past a circular cylinder (Mach 2): The pressure contour ranging from 0.0 to 4.2 (top panel) and density contour ranging from 0.054 to 3.2 (middle panel) and velocity magnitude distribution ranging from 0.0092 to 2.5 (bottom panel) at the spatial resolution  $dp = 1/20$ .

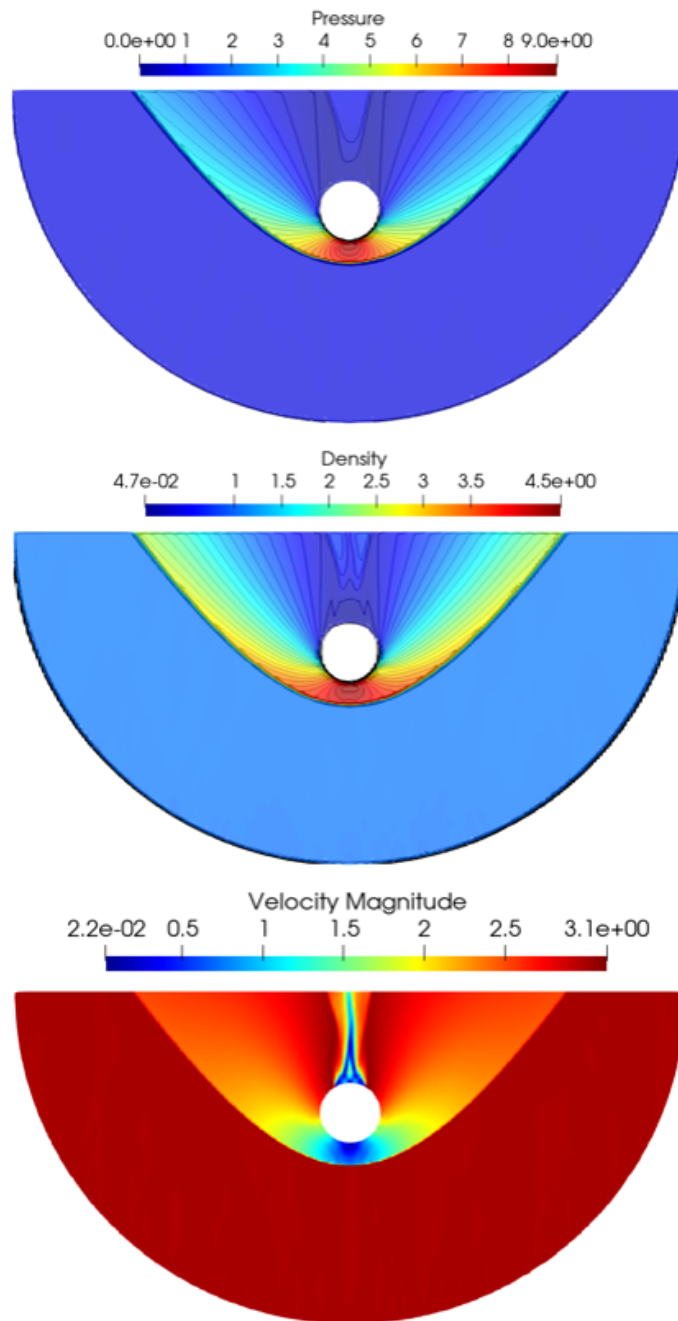


Figure 9: Supersonic flow past a circular cylinder (Mach 3): The pressure contour ranging from 0.0 to 8.9 (top panel) and density contour ranging from 0.047 to 4.5 (middle panel) and velocity magnitude distribution ranging from 0.022 to 3.1 (bottom panel) at the spatial resolution  $dp = 1/20$ .

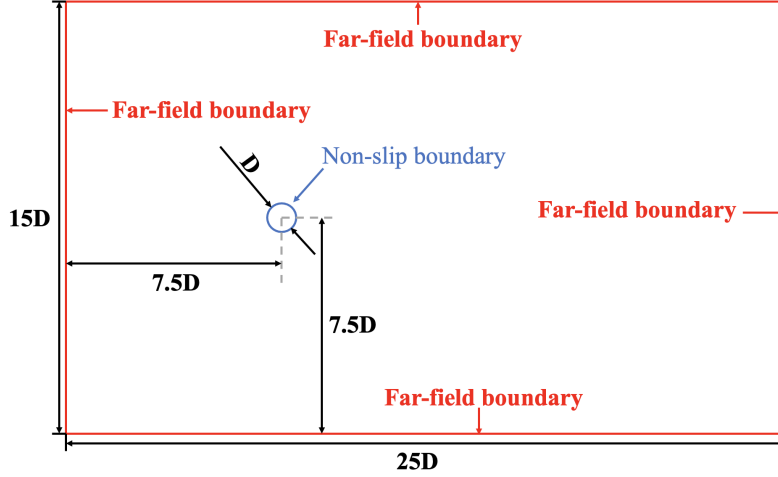


Figure 10: Flow around a circular cylinder: The geometry and boundary conditions.

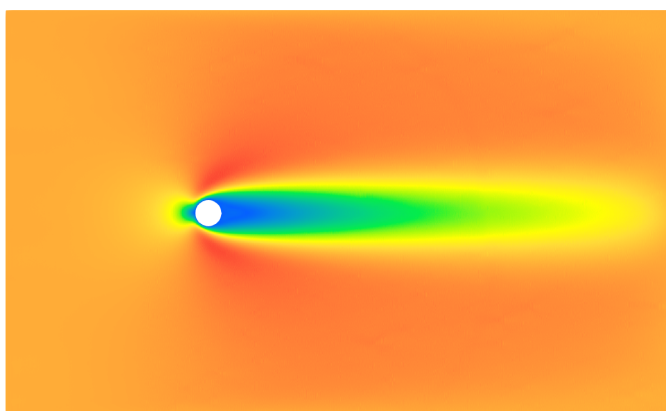
conditions, a computational domain of substantial size, namely  $[25D, 15D]$ , is employed. The center of the cylinder is positioned at  $(7.5D, 7.5D)$ , with the cylinder itself possessing a diameter of  $D = 2$ . To perform a quantitative analysis of the accuracy of the results, we employ drag and lift coefficients, which are defined as:

$$C_D = \frac{2F_D}{\rho_\infty u_\infty^2 A}, C_L = \frac{2F_L}{\rho_\infty u_\infty^2 A}. \quad (27)$$

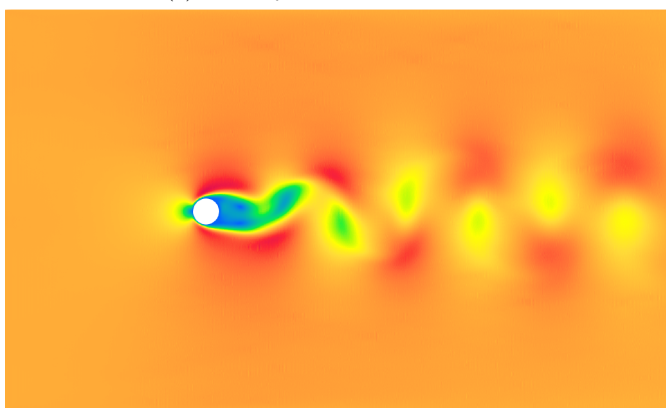
Here,  $F_D$  and  $F_L$  represent the drag and lift forces acting on the cylinder, respectively. Besides, a constant far-field velocity  $u_\infty$  and density  $\rho_\infty$  are both set to 1. Also, the Strouhal number  $St = fD/u_\infty$  with  $f$  the frequency in the unsteady cases and the Reynolds numbers  $Re = \rho_\infty u_\infty D/\mu$  are set as 100 and 200 in the case and the computational time is  $t = 300$ . For the convergence study, the spatial resolutions are applied as  $dp = 10, 20$ , and  $30$ .

Figure 11 portrays the velocity distributions ranging from  $6.0 \times 10^{-4}$  to 1.5 with the different Reynolds numbers including  $Re = 20, 100$  and  $200$  at the final time  $t = 300$ , showing that smooth velocity results with different Reynolds numbers can

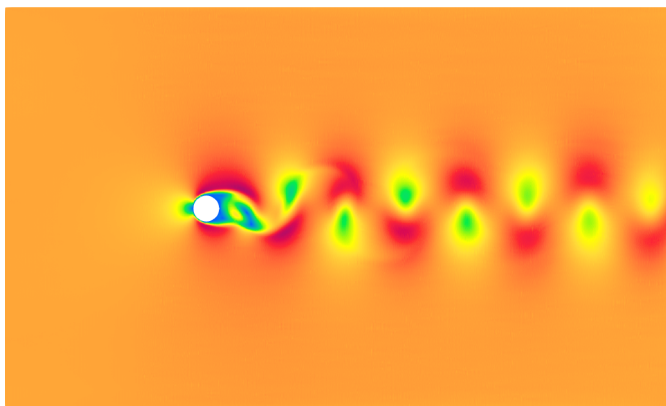




(a) The Reynolds number  $Re = 20$ .

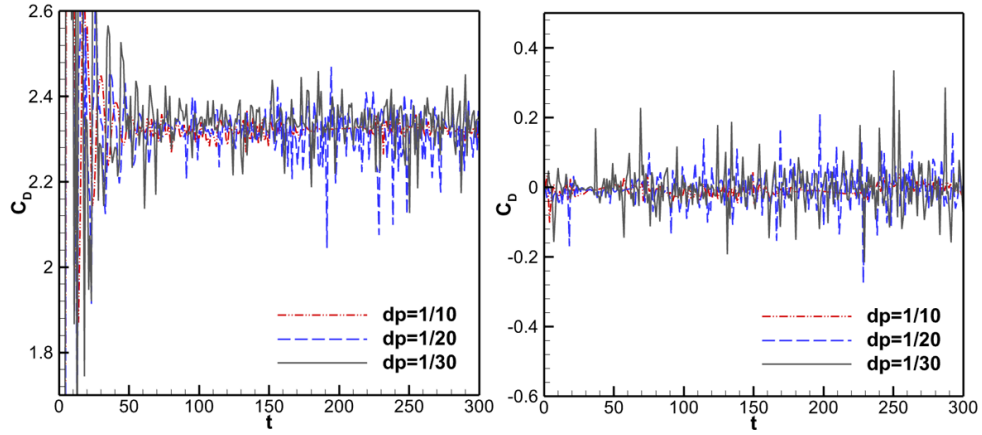


(b) The Reynolds number  $Re = 100$ .

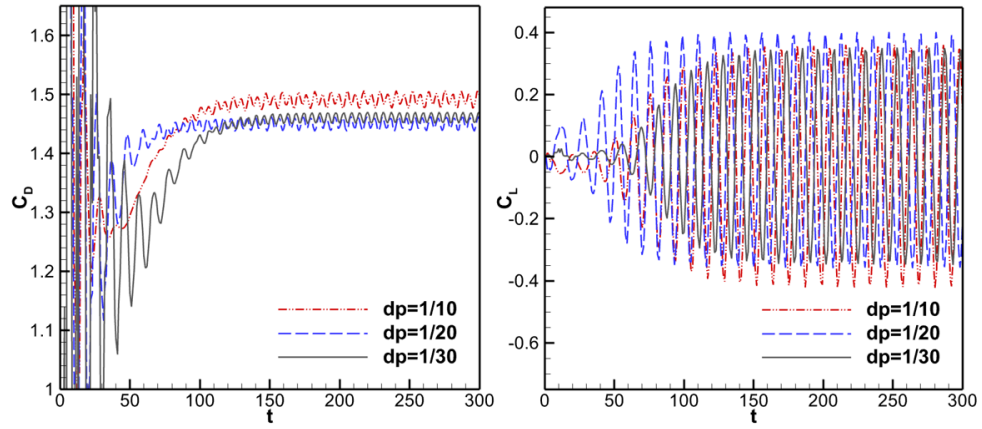


(c) The Reynolds number  $Re = 200$ .

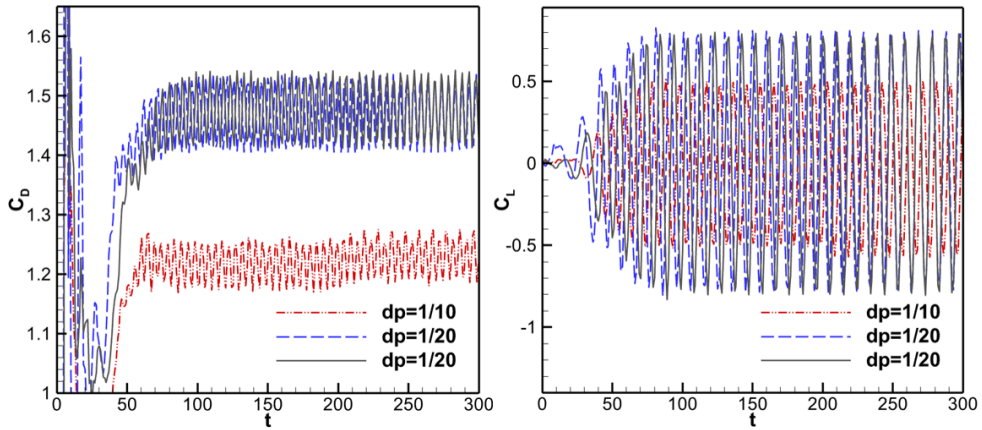
Figure 11: Flow around a circular cylinder: The velocity distributions ranging from  $6.0 \times 10^{-4}$  to 1.5 under the different Reynolds numbers at the final time  $t = 300$ .



(a) The Reynolds number  $Re = 20$ .



(b) The Reynolds number  $Re = 100$ .



(c) The Reynolds number  $Re = 200$ .

Figure 12: Flow around a circular cylinder: The convergence study of the drag and lift coefficients  $C_D$  and  $C_L$  under different Reynolds numbers with the spatial resolution  $dp = 1/30$ .

Table 1: Flow around a cylinder: Drag and lift coefficients from different experimental and simulation results with  $Re = 20$  and the result using the proposed boundary algorithm with the resolution  $dp = 1/30$ .

	$C_D$
Tritton [41]	2.09
Taira and Colonius [42]	2.06
Tafuni et al. [43]	2.29
Negi et al. [44]	2.32
Present	2.32

Table 2: Flow around a cylinder: Drag and lift coefficients from different experimental and simulation results with  $Re = 100$  and the result using the proposed boundary algorithm with the resolution  $dp = 1/30$ .

	$C_D$	$C_L$	$S_t$
White[45]	1.46	-	-
Chiu et al.[46]	$1.35 \pm 0.012$	$\pm 0.303$	0.166
Le et al.[47]	$1.37 \pm 0.009$	$\pm 0.323$	0.160
Brehm et al.[48]	$1.32 \pm 0.010$	$\pm 0.320$	0.165
Liu et al.[49]	$1.35 \pm 0.012$	$\pm 0.339$	0.165
Zhang et al.[33]	$1.61 \pm 0.005$	$\pm 0.448$	0.171
Present	$1.46 \pm 0.009$	$\pm 0.349$	0.176

Table 3: Flow around a cylinder: Drag and lift coefficients from different experimental and simulation results with  $Re = 200$  and the result using the proposed boundary algorithm with the resolution  $dp = 1/30$ .

	$C_D$	$C_L$	$S_t$
Taira et al. [42]	$1.35 \pm 0.048$	$\pm 0.68$	0.196
Tafuni et al. [43]	1.46	$\pm 0.693$	0.206
Negi et al. [44]	$1.524 \pm 0.05$	$\pm 0.722$	0.210
Jin and Braza [50]	$1.532 \pm 0.05$	$\pm 0.744$	0.210
Zhang et al.[33]	$1.63 \pm 0.05$	$\pm 0.84$	0.212
Present	$1.48 \pm 0.055$	$\pm 0.806$	0.208

be achieved by using the proposed algorithm. Also, the velocity distribution and the vortex street appeared during the simulation are agreement well with the results in Ref. [33]. Besides, with the increase of the resolutions from  $dp = 1/10$  to  $dp = 1/30$ , the results converge rapidly shown in Figure 12. It is observed that these plots reveal that the drag coefficients stabilize to a consistent mean value after an initial period of fluctuation, while the lift coefficient oscillates around zero. The deviations in the drag and lift coefficients for spatial resolutions of  $dp = 1/20$  and  $dp = 1/30$  remain below 3 percent, and the frequencies and amplitudes of the lift coefficient are approximately consistent. The converged results are listed in Tables 1, 2 and 3 which contains a series of numerical and experimental results with the Reynolds numbers  $Re = 20$ ,  $Re = 100$  and  $Re = 200$ , respectively. The observation shows that these results are agreement with the references in above Tables, validating that the proposed algorithm is convincing and accurate. In this study, the computations have been executed on a desktop computer equipped with an Intel Core i7-10700

processor, boasting 8 cores and a clock speed of 2.90 GHz. The total CPU wall-clock time consumed by the original boundary algorithm [29, 2], with the spatial resolution  $dp = 1/10$  and Reynolds number  $Re = 100$  throughout the entire process, amounts to 4141.94 seconds. However, the wall-clock time required by the proposed algorithm is 3600.63 seconds, showing its higher computational efficiency.

## 5. Summary and conclusion

In this paper, we firstly implement the particle relaxation technique in Eulerian SPH method generating the body-fitted particle distribution and satisfying the zero-order consistency of the particles not within the boundaries. By analysing the boundary algorithm in FVM, we propose the analogous algorithm in Eulerian SPH in detail and after implementation, the particles within the boundaries therefore also satisfy the zero-order consistency. Moreover, several numerical cases including fully and weakly compressible flows are tested and the results validate the stability and accuracy of the proposed algorithm. Another supplementary advantage lies in its potential to enhance computational efficiency to a certain degree.

## References

- [1] K. Mahady, S. Afkhami, L. Kondic, A volume of fluid method for simulating fluid/fluid interfaces in contact with solid boundaries, *Journal of Computational Physics* 294 (2015) 243–257.
- [2] Z. Wang, C. Zhang, O. J. Haidn, N. A. Adams, X. Hu, Extended eulerian sph and its realization of fvm, *arXiv preprint arXiv:2309.01596* (2023).

- [3] E. Napoli, M. De Marchis, C. Gianguzzi, B. Milici, A. Monteleone, A coupled finite volume–smoothed particle hydrodynamics method for incompressible flows, *Computer Methods in Applied Mechanics and Engineering* 310 (2016) 674–693.
- [4] S. Marrone, A. Di Mascio, D. Le Touzé, Coupling of smoothed particle hydrodynamics with finite volume method for free-surface flows, *Journal of Computational Physics* 310 (2016) 161–180.
- [5] P. Kumar, Q. Yang, V. Jones, L. McCue-Weil, Coupled sph-fvm simulation within the openfoam framework, *Procedia Iutam* 18 (2015) 76–84.
- [6] F. Afshari, H. G. Zavaragh, B. Sahin, R. C. Grifoni, F. Corvaro, B. Marchetti, F. Polonara, On numerical methods; optimization of cfd solution to evaluate fluid flow around a sample object at low re numbers, *Mathematics and Computers in Simulation* 152 (2018) 51–68.
- [7] J. O’connor, J. M. Domínguez, B. D. Rogers, S. J. Lind, P. K. Stansby, Eulerian incompressible smoothed particle hydrodynamics on multiple gpus, *Computer Physics Communications* 273 (2022) 108263.
- [8] J. Kim, D. Kim, H. Choi, An immersed-boundary finite-volume method for simulations of flow in complex geometries, *Journal of computational physics* 171 (1) (2001) 132–150.
- [9] F. Roman, E. Napoli, B. Milici, V. Armenio, An improved immersed boundary method for curvilinear grids, *Computers & fluids* 38 (8) (2009) 1510–1527.
- [10] C. Erath, A posteriori error estimates and adaptive mesh refinement for the coupling of the finite volume method and the boundary element method, *SIAM Journal on Numerical Analysis* 51 (3) (2013) 1777–1804.

- [11] S. Cheng, M. Zhang, Z. Chen, B. Wu, Numerical study of simultaneous growth of multiple hydraulic fractures from a horizontal wellbore combining dual boundary element method and finite volume method, *Engineering Analysis with Boundary Elements* 139 (2022) 278–292.
- [12] Z.-Y. Li, Z.-J. Chen, X.-H. Wu, W.-Q. Tao, Coupled mlp-g-fvm simulation of steady state heat conduction in irregular geometry, *Engineering Analysis with Boundary Elements* 100 (2019) 265–275.
- [13] L. Chiron, S. Marrone, A. Di Mascio, D. Le Touzé, Coupled sph-fv method with net vorticity and mass transfer, *Journal of Computational Physics* 364 (2018) 111–136.
- [14] R. A. Gingold, J. J. Monaghan, Smoothed particle hydrodynamics: theory and application to non-spherical stars, *Monthly notices of the royal astronomical society* 181 (3) (1977) 375–389.
- [15] L. B. Lucy, A numerical approach to the testing of the fission hypothesis, *Astronomical Journal*, vol. 82, Dec. 1977, p. 1013-1024. 82 (1977) 1013–1024.
- [16] J. J. Monaghan, Simulating free surface flows with sph, *Journal of computational physics* 110 (2) (1994) 399–406.
- [17] L. D. Libersky, A. G. Petschek, Smooth particle hydrodynamics with strength of materials, in: *Advances in the Free-Lagrange Method Including Contributions on Adaptive Gridding and the Smooth Particle Hydrodynamics Method: Proceedings of the Next Free-Lagrange Conference Held at Jackson Lake Lodge, Moran, WY, USA 3–7 June 1990*, Springer, 2005, pp. 248–257.

- [18] C. Zhang, Y. Zhu, D. Wu, X. Hu, Review on smoothed particle hydrodynamics: Methodology development and recent achievement, arXiv preprint arXiv:2205.03074 (2022).
- [19] H. Gotoh, A. Khayyer, Y. Shimizu, Entirely lagrangian meshfree computational methods for hydroelastic fluid-structure interactions in ocean engineering—reliability, adaptivity and generality, *Applied Ocean Research* 115 (2021) 102822.
- [20] S. Wang, J. Hu, C. Huang, Y. Yu, Graphics processing unit-accelerated smoothed particle hydrodynamics—finite difference method and the application for the flow around a cylinder with forced motions, *Physics of Fluids* 33 (12) (2021).
- [21] M.-K. Li, A. Zhang, F.-R. Ming, Y.-X. Peng, A coupled smoothed particle hydrodynamics-finite volume method for three-dimensional modeling of bubble dynamics, *Physics of Fluids* 35 (5) (2023).
- [22] R. Vacondio, C. Altomare, M. De Lefte, X. Hu, D. Le Touzé, S. Lind, J.-C. Marongiu, S. Marrone, B. D. Rogers, A. Souto-Iglesias, Grand challenges for smoothed particle hydrodynamics numerical schemes, *Computational Particle Mechanics* 8 (2021) 575–588.
- [23] C. Zhang, M. Rezavand, Y. Zhu, Y. Yu, D. Wu, W. Zhang, J. Wang, X. Hu, Sphixsys: An open-source multi-physics and multi-resolution library based on smoothed particle hydrodynamics, *Computer Physics Communications* 267 (2021) 108066.
- [24] C. Zhang, M. Rezavand, Y. Zhu, Y. Yu, D. Wu, W. Zhang, S. Zhang, J. Wang,



- X. Hu, Sphinxsys: An open-source meshless, multi-resolution and multi-physics library, *Software Impacts* 6 (2020) 100033.
- [25] J. Vila, On particle weighted methods and smooth particle hydrodynamics, *Mathematical models and methods in applied sciences* 9 (02) (1999) 161–209.
- [26] E. F. Toro, M. Spruce, W. Speares, Restoration of the contact surface in the hll-riemann solver, *Shock waves* 4 (1) (1994) 25–34.
- [27] E. F. Toro, The hllc riemann solver, *Shock waves* 29 (8) (2019) 1065–1082.
- [28] E. F. Toro, *Riemann solvers and numerical methods for fluid dynamics: a practical introduction*, Springer Science & Business Media, 2013.
- [29] Z. Wang, B. Zhang, O. J. Haidn, X. Hu, A fourth-order kernel for improving numerical accuracy and stability in eulerian and total lagrangian sph, *arXiv preprint arXiv:2309.01581* (2023).
- [30] Y. Zhu, C. Zhang, Y. Yu, X. Hu, A cad-compatible body-fitted particle generator for arbitrarily complex geometry and its application to wave-structure interaction, *Journal of Hydrodynamics* 33 (2) (2021) 195–206.
- [31] M. Neuhauser, Development of a coupled sph-ale/finite volume method for the simulation of transient flows in hydraulic machines, Ph.D. thesis, Ecully, Ecole centrale de Lyon (2014).
- [32] E.-S. Lee, C. Moulinec, R. Xu, D. Violeau, D. Laurence, P. Stansby, Comparisons of weakly compressible and truly incompressible algorithms for the sph mesh free particle method, *Journal of computational Physics* 227 (18) (2008) 8417–8436.

- [33] S. Zhang, W. Zhang, C. Zhang, X. Hu, A lagrangian free-stream boundary condition for weakly compressible smoothed particle hydrodynamics, *Journal of Computational Physics* (2023) 112303.
- [34] Z. Wang, C. Zhang, O. J. Haidn, X. Hu, An eulerian sph method with weno reconstruction for compressible and incompressible flows, *Journal of Hydrodynamics* (2023) 1–12.
- [35] P. Woodward, P. Colella, The numerical simulation of two-dimensional fluid flow with strong shocks, *Journal of computational physics* 54 (1) (1984) 115–173.
- [36] C.-Y. Wen, Y. Jiang, L. Shi, *Space–Time Conservation Element and Solution Element Method: Advances and Applications in Engineering Sciences*, Springer Nature, 2023.
- [37] J. Zhu, J. Qiu, A new type of finite volume weno schemes for hyperbolic conservation laws, *Journal of Scientific Computing* 73 (2017) 1338–1359.
- [38] D. Wang, X. Deng, G. Wang, Y. Dong, Developing a hybrid flux function suitable for hypersonic flow simulation with high-order methods, *International Journal for Numerical Methods in Fluids* 81 (5) (2016) 309–327.
- [39] Y. Zhu, X. Hu, Free-stream preserving linear-upwind and weno schemes on curvilinear grids, *Journal of Computational Physics* 399 (2019) 108907.
- [40] J. Sinclair, X. Cui, A theoretical approximation of the shock standoff distance for supersonic flows around a circular cylinder, *Physics of Fluids* 29 (2) (2017).
- [41] D. J. Tritton, Experiments on the flow past a circular cylinder at low reynolds numbers, *Journal of Fluid Mechanics* 6 (4) (1959) 547–567.

- [42] K. Taira, T. Colonius, The immersed boundary method: a projection approach, *Journal of Computational Physics* 225 (2) (2007) 2118–2137.
- [43] A. Tafuni, J. Domínguez, R. Vacondio, A. Crespo, A versatile algorithm for the treatment of open boundary conditions in smoothed particle hydrodynamics gpu models, *Computer methods in applied mechanics and engineering* 342 (2018) 604–624.
- [44] P. Negi, P. Ramachandran, A. Haftu, An improved non-reflecting outlet boundary condition for weakly-compressible sph, *Computer Methods in Applied Mechanics and Engineering* 367 (2020) 113119.
- [45] F. M. White, J. Majdalani, *Viscous fluid flow*, Vol. 3, McGraw-Hill New York, 2006.
- [46] P.-H. Chiu, R.-K. Lin, T. W. Sheu, A differentially interpolated direct forcing immersed boundary method for predicting incompressible navier–stokes equations in time-varying complex geometries, *Journal of Computational Physics* 229 (12) (2010) 4476–4500.
- [47] D.-V. Le, B. C. Khoo, J. Peraire, An immersed interface method for viscous incompressible flows involving rigid and flexible boundaries, *Journal of Computational Physics* 220 (1) (2006) 109–138.
- [48] C. Brehm, C. Hader, H. F. Fasel, A locally stabilized immersed boundary method for the compressible navier–stokes equations, *Journal of Computational Physics* 295 (2015) 475–504.
- [49] C. Liu, X. Zheng, C. Sung, Preconditioned multigrid methods for unsteady incompressible flows, *Journal of Computational physics* 139 (1) (1998) 35–57.

- [50] G. Jin, M. Braza, A nonreflecting outlet boundary condition for incompressible unsteady navier-stokes calculations, *Journal of computational physics* 107 (2) (1993) 239–253.